Electrodynamic magnetic levitation with discrete track Part II: Periodic track model for numerical simulation and lumped parameter model

Ove F Storset[1] and Bradley E Paden
Mechanical and Environmental Engineering Department,
University of California, Santa Barbara,
CA 93106-5070, U.S.A.
Email[1]: ove.storset@ieee.org

September 30, 2005

Abstract

This paper presents time dynamic numerical models for discrete track electrodynamic suspended (EDS) magnetic levitation (maglev). In contrast to typical simulation models, we base our equations on precise derivations from Maxwell's equations, and provide an explicit bound on the error that arise from the dimension reduction to an ordinary differential equation (ODE) in terms of the numerical error. The end effect is accounted for by resetting the state, and the source magnetic field is incorporated in spline interpolation tables for fast numerical evaluation. From this ODE, we derive a lumped parameter model, clearly stating the underlying assumptions, and show the similarity with the thin sheet high speed approximation model for continuous track EDS maglev. We also demonstrate the inherent inaccuracy in the lumped parameter model from comparison with the numerical model.

1 Introduction

This paper presents numerical models for electrodynamic suspended (EDS) magnetic levitation (maglev), where a repulsive levitation force is created between a moving magnetic source and currents induced in a conductive guideway. We further limit the presentation to discrete tracks, which employs structured conductors as shown in Figure 1, and will not cover continuous sheet tracks nor electromagnetic suspensions.

EDS has intricate dynamics, with modes of the linearization that are easily perturb across the imaginary axis under approximations. It is therefore essential to maintain precision in dynamic currents and forces in the simulation models. For a maglev vehicle with 6DOF and multiple reference frames, this is especially important since the 3D electromagnetic geometry creates complex dynamics with numerous terms that are difficult for the designer to keep track of. In addition, the low dissipation in EDS gives rise to periodic phenomena like limitcycles and bifurcations that are undetected by simplified models. For these reasons, it is imperative to have a precise, efficient simulation environment to evaluate different designs.

Multiphysics based, 3D, time dynamic FEM simulations are inappropriate, mainly due to the large computational expense of moving objects explained in [1]. This paper serve to fill this lack of computational efficient simulation models for EDS maglev, and is based on the Infinite Track Model (ITM) derived in [1]. A comprehensive literary review is also included in [1].

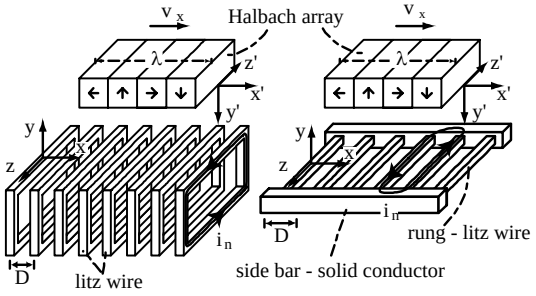

Figure 1: Examples of discrete track systems. Window framed track (left) and ladder track (right) with single-sided Halbach array as source.

1.1 Motivation

Discrete track models are typically based on approximations with little regard to coherence with Maxwell's equations [1], and most of these models utilizes constant propulsion speed and constant levitation height and are therefore not dynamic. Those models that are time dynamic tend to be rudimentary with fixed damping and spring constants like [2].

Maglev dynamics have traditionally been modelled using rotating electric machine theory (REMT) utilizing inductance for flux interactions computed from filament current considerations; forces are computed as the gradient of mutual inductances. For rotating machinery there is no end effect, and only a finite number of currents in the dynamic model suffice. Maglev, however, is linear machinery, and by employing a finite number of filament conductors, the vehicle "runs out of track" after a certain time. To evaluate the stability of the resonant frequencies (typically around 1-3 Hz), the models must incorporate excessively many conductors to capture the growth or decay of the oscillations. Therefore, REMT models have limited use, especially for densely spaced tracks. In addition, some mean must be provided to account for the eddy currents that might seem insignificant from a power loss perspective, but are crucial for the dynamics since they damp oscillatory motion [3],[4].

Early numerical models for continuous track EDS [5] utilized GREMT, and were used to investigate the rigid vehicle dynamics under perturbations such as wind gusts and guideway irregularities, with little emphasis on the dynamic precision of the magnetic forces that were computed from the inductance between the magnetic source and the sheet track—coined "impedance modelling" in [6][1].

[1] See [1] for more references on impedance modelling.

To adapt this model to discrete tracks, it is necessary to include the individual track currents as states as done in [7] to evaluate the sidewall mounted null-flux system for levitation, guidance and propulsion [8], that is a pre-runner to the present MLX series of vehicles at the Yamanashi test track in Japan (RTRI).

An improved version of this REMT model is provided in [9],[10],[11]. The authors compute the inductances from 2D Fourier series expansions of the source, increasing the force accuracy relative to inductances computed from filament current sources, allowing sufficient interspace to include the end effect. The inductances are then incorporated into interpolation tables for fast numerical evaluation. However, the authors are unclear concerning the implementation of the tables, which are functions of all the degrees of motion to retain dynamic correctness.

Contrary to [11], [12] provides a model incorporating eddy losses in the cryostat shielding plates to determine the damping of the MLX series of vehicles (RTRI), but is vague concerning the inductance computations. Another dynamic model on the MLX series of vehicles is [13], which utilizes stiffness and damping coefficients as functions of several parameters. However, besides ignoring end effect, the authors make the typical error of forgetting to include heave velocity in the stiffness and damping models, which is vital for correct dynamic behavior [4].

In [14], 25 years of maglev research pertaining to factors that influence dynamic stability is summarized, and the authors conclude with the need for numerical simulation models capable of screening designs. To, bridge this gap, we propose our Periodic Track Model (PTM), and to our knowledge, this is the first time there is a systematic approach to retain dynamic correctness for discrete track EDS in a dynamic simulation model. In addition, we provide a solution to "running out of track" particularly important for densely spaced tracks.

Lumped parameter models (LPMs) were used in the infancy of maglev technology as the semiquantitative calculations in [15]. Due to the simplicity of such models, lumped track inductance and resistance were also utilized in [16] and [17] with little experimental corroboration. Lately, LPMs have been applied in [18] to model the densely spaced, discrete track maglev system labeled Inductrack. However, little has been done to unify LPM models, and even fewer papers have clarified their limitations.

We clearly state the underlying assumptions of the LPM's, and explain their limitations relative to more accurate models. But despite their inaccuracies LPMs provide useful concept for building intuition.

2 Our contribution

We investigate simulation models for *discrete track EDS* under *quasistatic magnetic conditions* restricted to magnetic sources with low conductivity[2]. The methods employed provide a general framework for all discrete tracks geometries like single loop, double loop, null-flux or ladder track composed of *stranded conductors* (litz wire) or solid conductors with *linear conducting material* and a *spatial periodic geometry* in the propulsion direction with small deviations in electric properties. Our modelling approach can be generalized to 6DOF, and the analysis is applicable to all linear machinery under similar assumptions.

Based on the *infinite track model* (ITM) presented in [1], we derive a *periodic track model* (PTM) for numerical simulation preserving the dynamic and static properties of the ITM with a predesignated bound on the deviation error that can be made arbitrarily small.

The purpose of the PTM is to maintain the dynamic accuracy of the ITM with minimal computational efforts. This requires a careful system reduction since maglev dynamics have modes of the linearization that are easily perturbed across the imaginary axis under approximations, and great care must be exercised to assure that the lower dimensional PTM retain the properties of the ITM. The approach outlined here can be extended to 6DOF vehicle dynamics with minor modifications.

The PTM has been implemented in the Simulink/Matlab$^{\mathrm{TM}}$ environment in C-code with 2DOF, allowing dynamic propulsion and disturbance force inputs, and is intended for dynamic design verification of forces and currents. The implementation of the PTM is prepared for actuator coils for active heave control. This model implementation has been used to validate the ITM model against the rotating wheel experiment to General Atomics of San Diego, which is reported in [19]. The Simulink environment provides flexibility in constructing complex models from simple sub-blocks, and the PTM provides the magnetic interaction sub-block as the fundamental part of larger models as for instance a maglev vehicle with secondary suspension with force interaction from multiple boogies with several PTM sub-blocks.

[2] We allow for an auxilary control current in high conductivity material in the source field.

Subsequently, we present a *lumped parameter model* (LPM), neglecting the end effect of the track and the source magnetic field that provides simple equations for baseline design with less accuracy than the ITM. Although the essential heave dynamics can be retained in the LPM by time-scale analysis, we only present a static force LPM valid under *constant levitation height*, parameterized by a *constant propulsion speed*, and have relegated the dynamics to another investigation [20].

2.1 Organization

Later in this Section notation and nomenclature is presented. The ITM is briefly explained in Section 3.1, and is truncated to a finite set of track currents in Section 3.2 according to a given criterion for force accuracy. This order reduction amends some conditioning of the magnetic field which is explained in Section 3.3. Thereafter, an interpolation table is constructed from splines for fast numerical evaluation of the source magnetic field in Section 3.4, and the necessary alterations of the ITM operators are described in Section 3.5. The PTM with execution algorithm is presented in Section 4, and essential details of the spline fitting procedure is given in Section 4.2. The properties of the PTM is shown in simulations in Section 4.3.

The underlying assumptions of the Lumped parameter model is precisely stated in Section 5, and the necessary modifications of the magnetic field is performed in Section 5.1. The track equivalent resistance and inductance are derived in Section 5.2, and finally the static forces of the PTM parametrized by propulsion velocities are presented in 5.3. We provide a comparison between the PTM and the LPM in Section 6, and summarize our findings in Section 7

2.2 Nomenclature and Notation

The coordinate systems are oriented as in Figure 1, with the x-axis as the horizontal or *propulsion direction*; the y-axis is the vertical or *levitation direction*, while z is directed *transverse* to the track in the lateral direction. We reserve superscripts for name labeling as $\mathbf{B}^s$ and i^{loop}, and use subscript for number indexing like i_n and i_{m+1}. Calligraphic $\mathcal{B}$ represent magnetic flux density integrated transversely as $\mathcal{B}(x,y) \triangleq \int_{-w/2}^{w/2} \mathbf{B}(x,y,z)dz$; moreover, when no ambiguity can arise, we refer to the magnetic flux density vector $\mathbf{B}$ as "the magnetic field", which is justified by the constant permeability $\mathbf{B} = \mu_0 \mathbf{H}$. Scalar component functions are denoted with lower indices $\mathcal{B} = (\mathcal{B}_x, \mathcal{B}_y, \mathcal{B}_z)$, such that $\mathcal{B}_x \triangleq \mathcal{B} \cdot \hat{\mathbf{e}}_x$, where '$\cdot$' is vector (inner) product in $\mathbb{R}^3$. Curly braces are used to denote bi-infinite vectors $\{i_n\} \triangleq \{\ldots, i_{-2}, i_{-1}, [i_0], i_1, i_2, \ldots\} = i\{n\} = i\{n\}(t)$, where the square bracket identifies term number zero. The inner product between $a\{n\}$ and $b\{n\}$ is defined as $\langle \{a_n\}, \{b_n\} \rangle_n \triangleq \sum_{n=-\infty}^{\infty} a_n b_n$. Finite dimensional vectors are denoted using regular braces as $(i_1, \ldots, i_{\mathcal{N}}) = i_{\mathcal{N}}(n) = i_{\mathcal{N}}(n)(t)$. We use t_m^- to distinguish the event at simulation time t_m associated with the time interval $[t_{m-1}, t_m]$ as distinct from the event t_n^+ related to the next interval $[t_n, t_{n+1}]$.

Some quantities are explained in Appendix 9.1 and have been removed from the nomenclature given here.

Symbol	Interpretation
$\mathbf{F} = (F^d, F^l, 0)$	dynamic force between levitated object and the track
F^d	drag force
F^l	lift force
$\mathbf{F}^{in}$	propulsion force
$\boldsymbol{\alpha}^{par}$	parasitic dissipation (damping) coefficient
$\boldsymbol{\alpha}^{m}$	mechanical damping coefficient
i, i_n	arbitrary filament current
y	distance from lower edge of array to the vertical center of the rung
y_ϕ	effective flux levitation height
y_F	effective force levitation height
$\mathcal{N} = 2N + 1$	loop currents in the periodic track model
$\Gamma^x(nD)$	infinite dimensional track sampling operator
$\Gamma^x_{\mathcal{N}}(nD)$	truncated track sampling operator
L	self-inductance of a track loop
M_k	mutual inductance between loops k loops apart
$\{l_n\}$	inductance vector
R^T	rung termination resistance
$\mathcal{L}$	track inductance matrix for the ITM
$\mathcal{L}_{\mathcal{N}}$	track inductance matrix for the PTM
$\mathcal{R}$	track resistance matrix for the ITM
$\mathcal{R}_{\mathcal{N}}$	track resistance matrix for the PTM
$\mathbf{B}^s, \mathcal{B}^s$	magnetic source field
$\mathbf{B}^{sP}, \mathcal{B}^{sP}$	spline fit of the magnetic source field
N^λ	number of conductors below a wavelength of Halbach array

3 Periodic track model for numerical simulation

This exposition is based on the derivation of the ITM in [1], but we provide a brief summary here for completeness. Electrodynamic suspended maglev is described by a PDE labeled the (track) *current equation* (1) coupled to an ODE named the (force) *mechanical equation* (2)-(3) determining the movement of the body. For brevity, motion is constrained to heave (levitation) in the y-direction and propulsion dynamics in the x-direction as indicated in Figure 1, where (x, y, z) are coordinates in the inertial frame, and (x', y', z') in the moving frame.

3.1 Infinite track model

The equations (1)-(3) represent any track configuration like ladder track, single loop, double loop, or null-flux. However, we specialize to the ladder track, assumed infinite in both directions, described by the bi-infinite loop current vector $i\{n\} \triangleq \{\ldots, i_{-2}, i_{-1}, [i_0], i_1, i_2, \ldots\}$.

The track rung conductors are stranded (litz wire), and the *filament current approximation* gives rise to the *effective flux levitation height* $y_\phi \triangleq y - \Delta y_\phi$, where Δy_ϕ is an offset from the levitation height y measured between the center of a rung and the lower edge of the source magnetic field, whereas the *effective force levitation height* $y_F \triangleq y_0 - \Delta y_F$ is measured in a similar fashion with Δy_F as offset. *The horizontal increase in the flux window* $\Delta\phi$ from the center of the conductor is introduced to capture the increased flux the 3D geometry of the a litz wire loop experience compared to a filament loop as explained in [1], and is necessary to yield correct lift and drag forces for double-sided magnetic sources $\mathbf{B}^s$.

Eddy currents in conductor strands, solid conductors and surrounding material are accounted for using power loss labeled *parasitic dissipation* through the parasitic drag force $\alpha_x^{par} dx/dt$ and the parasitic heave damping $\alpha_y^{par} dy/dt$.

The track resistance and inductance are captured by the *circulant symmetric*, infinite dimensional $\mathcal{L}$ and $\mathcal{R}$ matrices, and the *stationary current vector field pattern* implicitly presumed by inductance modeling, is relieved by parameterizing the matrix entries with propulsion speed.

The source magnetic field $\mathbf{B}^s$ integrated transversely over the track width w has component functions $\mathcal{B}^s_k(x', y')$; $\mathbf{F}^{in}$ is a propulsion force; m is the vehicle mass; g is the acceleration of gravity, and $\alpha_x^m dx/dt$ and

$\alpha_y^m dy/dt$ are mechanical damping forces. The ITM is described by

$$\begin{aligned}
\frac{d}{dt} i\left\{n\right\} &= -\mathcal{L}^{-1}\mathcal{R} i\left\{n\right\}(t) + \mathcal{L}^{-1}\Gamma^x_{\Delta\phi}\left\{nD\right\}\mathcal{B}^s_y(x,y_\phi)\frac{dx}{dt} \\
&\quad -\mathcal{L}^{-1}\Gamma^x_{\Delta\phi}\left\{nD\right\}\int \frac{\partial}{\partial y}\mathcal{B}^s_y(x',y_\phi)dx'\frac{dy}{dt} \qquad (1) \\
\frac{d^2x}{dt^2} &= \frac{1}{m}\left\langle \Gamma^x\left\{nD\right\}\mathcal{B}^s_y(x,y_F), i\left\{n\right\}(t)\right\rangle_n - \frac{1}{m}\left(\alpha_x^{par}+\alpha_x^m\right)\frac{dx}{dt} + \frac{1}{m}F_x^{in} \qquad (2) \\
\frac{d^2y}{dt^2} &= -\frac{1}{m}\left\langle \Gamma^x\left\{nD\right\}\mathcal{B}^s_x(x,y_F), i\left\{n\right\}(t)\right\rangle_n - \frac{1}{m}\left(\alpha_y^{par}+\alpha_y^m\right)\frac{dy}{dt} + \frac{1}{m}F_y^{in} - g, \qquad (3)
\end{aligned}$$

where the *track sampling operator* $\Gamma^x\left\{nD\right\}$ exploits the *spatial periodic geometry of the track* in the x-direction, and samples the magnetic field at an infinite number of positions with lattice constant D as

$$\begin{aligned}
\Gamma^x\left\{nD\right\}f(x,y_\phi) &\triangleq \bigotimes_{n=-\infty}^{\infty} f(nD-x',y_\phi)\big|_{x-D}^{x'=x} \\
&= \left\{\ldots, f(-D-x',y_\phi)\big|_{x-D}^{x'=x}, \left[f(-x',y_\phi)\big|_{x-D}^{x'=x}\right], f(D-x',y_\phi)\big|_{x-D}^{x'=x}, \ldots\right\}. \qquad (4)
\end{aligned}$$

By increasing each flux conductors window horizontally direction by $\Delta\phi$ at either side, we get $\Gamma^x_{\Delta\phi}\{nD\}$ defined as

$$\Gamma^x_{\Delta\phi}\{nD\}f(x,y_\phi) \triangleq \bigotimes_{n=-\infty}^{\infty} f(nD-x',y_\phi)\big|_{x-D+\Delta\phi}^{x'=x-\Delta\phi}. \qquad (5)$$

Unfortunately, this model is infinite dimensional, suitable for harmonic analysis, but is inefficient for numerical evaluation. The dimension reduction to a finite dimensional ODE creates several issue which must be overcome.

3.2 Truncating the ITM to a periodic track

The force between the magnetic source $\mathbf{B}^s$ and the track is determined arbitrary precise by including sufficiently many track loops in front and rear of the levitated vehicle. For each time instant, given a maximum force error ϵ, there is a minimum number of track loops $\mathcal{N}^F$ which will provide the required accuracy, or more precise

$$\forall\epsilon, \exists\mathcal{N}^F \quad N > \mathcal{N}^F \;\Rightarrow\; |\mathbf{F}-\mathbf{F}_N|_{l_1} \le \sum_{|n|>N/2} |\mathbf{i}_n \times \mathcal{B}^s| < \epsilon, \qquad (6)$$

here $\mathbf{F}_N$ is the force from the $\mathcal{N}^F = 2N^F+1$ conductors with the largest partial force, whereas $\mathbf{F}$ is the force from all conductors, and $|\{a_n\}|_{l_1} = \sum_{n=-\infty}^{\infty}|a_n|$. This *force continuity criterion* guarantees a similar dynamic behavior between the ITM and the truncated PTM if ϵ is sufficiently small.

There are complications however, since the moving vehicle quickly runs away from the N stationary track conductors. To circumvent this, we "recycle" the track from the rear to the front, similar to a tracked vehicle, after discharging the current i_0 as shown in Figure 2.

The *spatial periodic geometry* makes the track *shift invariant* in the x-direction with D as the *wavelength of the track*, which is the distance between the horizontal center of each rung for the ladder track in Figure 1. A track with $\mathcal{N}^F$ track conductors as "holders" for $\mathcal{N}^F$ track currents i_n has the following propulsion algorithm to circumvent running out of track: After the levitated object has moved the distance $x(t_1^-) = D$ in the time interval $[t_0, t_1]$, all currents are propagated one conductor backwards; the last current i_1 is circulated from the rear to the *discharge position* i_0, and i_0 is propagated to the foremost current $i_{\mathcal{N}}$, as shown in Figure 2. Simultaneously at t_1, the distance traveled is set to zero $x(t_1^+) = 0$, and the *interval number* counter m_x is incremented. In this manner, there has not been any relative movement between the levitated vehicle and the currents. The only difference between t_1^- and t_1^+ is the removed current $i_1(t_1^-)$ and the inserted current $i_{\mathcal{N}}(t_1^+)$. The process is repeated after the vehicle has moved another distance $x(t_2^-) = D$.

If the rearmost current i_1 were discharged instantaneously at $t = t_m$, we would get an ODE $dz/dt = f(z)$ with discontinuous right hand side in the sense of Filipov [21], and the equations would be difficult to solve numerically as $f(z(t_m))$ fails to be Lipschitz continuos. Instead, we use a *discharge coefficient* α such that

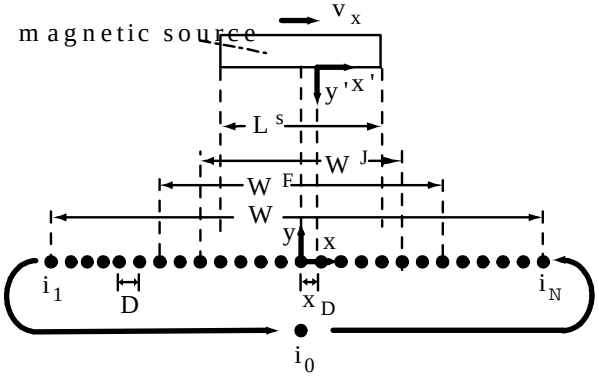

Figure 2: Periodic track model with the corresponding track current windows for the source W^J, force W^F and track W.

$di_0/dt = -\alpha\, dx/dt\, i_0$, and reduce i_0 to less than the numerical accuracy in the interval $[t_m, t_{m+1}]$. Thus, the only source of force error is the removed rearmost current $i_1(t_1^-)$ which is kept small by fixing $\mathcal{N}^F$ sufficiently large in accordance with (6).

The *magnetic source window* W^J, as seen in Figure 2, contains the $\mathcal{N}^J$ track conductors that are directly under the source current region L^s at $x_D = 0$ plus two more conductors to allow for the movement D. The *force window* W^F with $\mathcal{N}^F = 2N^F + 1$ conductors determined by (6) is not much wider than W^J as diffusion and dissipation quickly weakens the currents i_n outside the magnetic source window as shown in Figure 8.

From the narrowness of the force window W^F three issues arises. First, the currents just outside W^F are significant relative to numerical accuracy requiring a large discharge coefficient α, making a stiff[3] ODE that is unnecessary computationally demanding. Secondly, we only get a truncated loop current time profile out of the model since the currents are discharged. Thirdly, the slowly decaying magnetic far fields provides a significant excitation far out to the sides as explained in Section 3.3. For these three reasons we extend the number of conductors to $\mathcal{N} = 2N + 1$ labeled the *track window* W, so that the PTM's current state is

$$i_{\mathcal{N}}(n,t) = i_{\mathcal{N}}(n) \triangleq (i_1, ..., i_{\mathcal{N}})\,, \tag{7}$$

as shown in Figure 2.

Due to the resetting of distance travelled $x(t)$ at time instances $t_1, t_2, \ldots, t_m, \ldots$, the PTM employs x_D which is the distance traveled modulus D

$$\begin{array}{l} x_D \triangleq (x)_{\mathrm{mod}\, D}, \quad 0 \le x_D(t) \le D \\ x = x_D + m_x D, \end{array} \tag{8}$$

where m_x is the *interval number*. Notice that we define $dx_D/dt \triangleq d/dt(x_D + m_x D)$ to avoid continuity problems, and that $dx_D/dt \equiv dx/dt$.

3.3 Modification of the source magnetic field for the periodic track - attenuating the tails

The source magnetic field $\mathbf{B}^s(\mathbf{p}')$ is determined by Poisson's Equation $\Delta \mathbf{A}^s = -\mu_0 \mathbf{J}^s$, an elliptic PDE with far fields that decay very slowly. Consequently, the tails of $\mathcal{B}_x^s(x', y')$, and $\mathcal{B}_y^s(x', y')$ are significant far out to the sides of the source $\mathbf{J}^s$. For instance, if the horizontal termination of the a Halbach array as shown in Figure 1 has magnetization in the vertical ($\hat{\mathbf{e}}_y$) direction only, we employ Gauss Law for magnetic fields $\oint_V \mathbf{B}^s \cdot d\mathbf{S} = 0$ with a closed surface V extending far out to the sides and containing the array termination, to observe that

$$0 < |B_x^s(x', y', z')| << \left|B_y^s(x', y', z')\right|, \quad x' >> y' + z', \tag{9}$$

[3] A "stiff" ODE $dz/dt = f(z)$, has a large separation between a fast time-scale and a slow time-scale such that the eigenvalues of the linearization $\lambda_n(\nabla f(z))$ have very different magnitudes, or $|\lambda_{\min}(\nabla f(z))| \ll |\lambda_{\max}(\nabla f(z))|$.

so that B_y^s is significant even far out to the sides. This has no influence on force continuity (6), but creates tails of i_n that are truncated without converging to zero. Hence, when the currents i_n are propagated backwards, the removed current i_1 is significant and the solver attempts to reduce the numerical error by shortening the time step size requiring more computation time. To prevent this, we attenuate the tails of $\mathcal{B}_k^s(x', y')$ as shown in Figure 3 starting at the ends of the force window W^F, so that the field is sufficiently attenuated at the termination of the track window W.However, we must ensure that the attenuated field

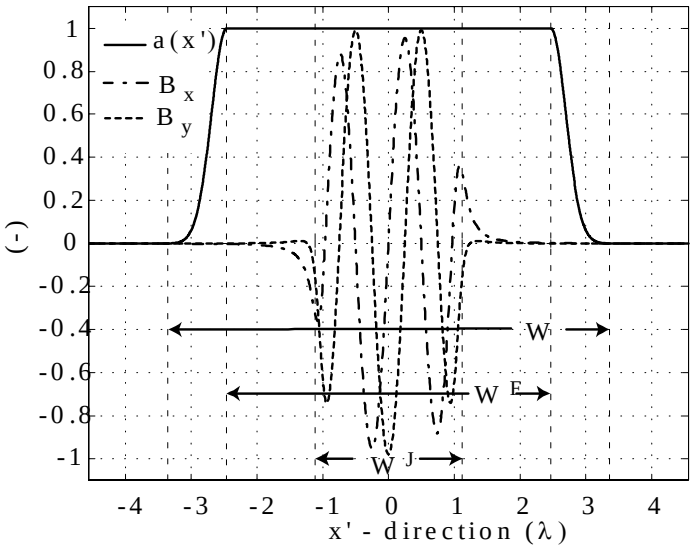

Figure 3: Attenuating function $a(x')$ shown together with $B_x^s(x', y' = 34mm)$ and $B_y^s(x', y' = 34mm)$ for the one sided array. See Appendix 9.1 for details.

$\mathbf{B}^{cut}(x', y', z') = \mathbf{B}^s(x', y', z')a(x')$ is sufficiently smooth to avoid large excursions in the partial derivatives of B_k^{cut} at the onset of the cut. The multiplicative *attenuation function* $a(x')$ (shown in Figure 3) achieve this by a Gaussian $e^{-x^2/2\sigma^2}$producing a smooth transition at the onset of the cut as

$$a(x') = \begin{cases} e^{-\frac{(x'+\mu)^2}{2\sigma^2}}, & x' \leq -\mu \\ 1 & -\mu < x' < \mu \\ e^{-\frac{(x'-\mu)^2}{2\sigma^2}}, & x' \geq \mu, \end{cases} \tag{10}$$

where $\mu = W^F/2$, and the parameter σ (referred to as "standard deviation" in statistics) is chosen to make $a(\pm\mu)$ sufficiently small.

3.4 Magnetic field for numerical evaluation - spline fit

Solving the ITM numerically requires evaluating the source magnetic field $\mathcal{B}_k^s(x', y')$ efficiently which eliminates solving Poisson's equation $\Delta\mathbf{A}^s = -\mu_0\mathbf{J}^s$ at each time step. An analytic solution to Poisson's equation is usually attainable for source currents $\mathbf{J}^s$ with simple geometric shapes such as current sheets [22],[23]. However, these solutions contain transcendental functions, which number increase with the source complexity, and evaluate in a FPU roughly 100 times slower than addition and multiplication. It is therefore not recommended to employ analytical solutions in real time.

To overcome this computational bottleneck, we apply spline approximations $\mathcal{B}_x^{sP}$and $\mathcal{B}_y^{sP}$ of the transversely integrated magnetic source field $\mathcal{B}_x^s$ and $\mathcal{B}_y^s$, respectively. With only 2DOF (x', y'), the magnetic field from a Halbach array is almost separable such that $\mathcal{B}_k^s(x', y') \simeq f_k(x')g_k(y')$ as shown in Figure 4.The approximate separability allows performing the spline fit on a rectangular grid determined by the *break point sequences*

$$(\xi_i)_{K+1} \triangleq \xi_1, \xi_2, \xi_3, \ldots, \xi_{K+1} \tag{11}$$

$$(\zeta_i)_{J+1} \triangleq \zeta_1, \zeta_2, \zeta_3, \ldots, \zeta_{J+1}, \tag{12}$$

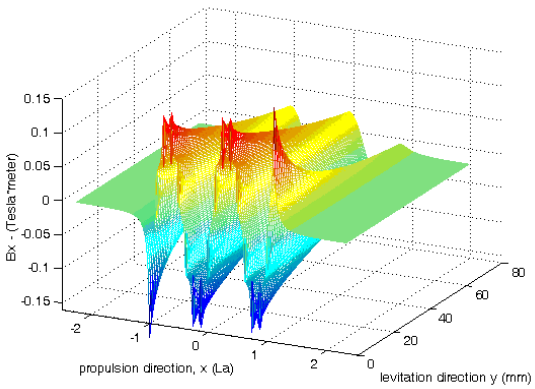

Figure 4: Transversely integrated magnetic field $\mathcal{B}_x^s = \int_{-w/2}^{w/2} B_x^s(x,y,z)dz$ for the single sided array shown in Figure 8 with technical details in Appendix 9.1. Notice the high spatial frequency components close to the magnetic source.

in the x- and y-direction respectively and nevertheless have reasonably good control of the approximation error $\left|\mathcal{B}_k^s - \mathcal{B}_k^{sP}\right|$.

For efficient spline evaluation, we choose tensor product splines in the *piecewise polynomial form* (*pp-form*). Tensor product splines also simplifies the code used to create and evaluate a 2D spline by reapplying a 1D spline procedure [24], which reduces software development time. The disadvantage of tensor product splines is that the breakpoint sequences (ξ_i) and (ζ_i) must be very carefully adapted to $\mathcal{B}_k^s(x',y')$ to create a small approximation error. Therefore, the fit of $\mathcal{B}_x^{sP}$and $\mathcal{B}_y^{sP}$ are made on separate grids. In conclusion, the numerical implementation of the PTM requires spline fits of $\mathcal{B}_x^{sP}$, $\mathcal{B}_y^{sP}$ and $\partial\mathcal{B}_y^{sP}/\partial y$ with further details in Section 4.2.

For a general magnetic source field $\mathbf{B}^s$ the component functions $\mathcal{B}_k^s(x',y') : \mathbb{R}^2 \to \mathbb{R}$ are not necessarily separable. In addition, for a 6DOF maglev vehicle with sway z (sideways) movement in addition to the rotations: roll ψ (around the propulsion or x-axis), pitch φ (around lateral or z-axis) and yaw θ (around the vertical y-axis), yield flux component functions $B_k^s(x',y',z',\psi',\varphi',\theta')$ of six variables $B_k^s : \mathbb{R}^6 \to \mathbb{R}$. Here, approximate separability $B_k^s \simeq \prod_n f_n(x_n)$ is seldom the case, and in order to obtain acceptable approximation errors $\left|B_k^s - B_k^{sP}\right|$, it is necessary to segment the six-dimensional domain based on the values of B_k^s [4], and it is not feasible to use a rectangular grid for such problems.

3.5 Periodic track operators - modifications from ITM

For the ladder track, the truncation of the track into $\mathcal{N}$ conductors diminish the resistive dissipation, and the currents persists longer at the ends due to the missing parallel resistance of the removed loops. To avoid changing the track dissipation, the leftmost and the rightmost rung resistance R_r is set to R_T

$$R_T \triangleq R_r || \left(2R_b + R_r || \left(2R_b + R_r || \left(2R_b + R_r || \cdots\right)\right)\right), \tag{13}$$

which is the equivalent track resistance to one side of an infinite track. This modification provides the same equivalent track resistance in both directions for all rungs, and by defining $R' = R_T + R_r + 2R_b$, the $\mathcal{N}$-by-$\mathcal{N}$ track resistance matrix $\mathcal{R}_\mathcal{N}$ is

$$\mathcal{R}_\mathcal{N} = \begin{bmatrix} R' & -R_r & \dots & 0 & 0 \\ -R_r & 2\left(R_r + R_b\right) & \ddots & 0 & 0 \\ \vdots & \vdots & \ddots & \vdots & \vdots \\ 0 & 0 & \ddots & 2\left(R_r + R_b\right) & -R_r \\ 0 & 0 & \dots & -R_r & R' \end{bmatrix}, \tag{14}$$

[4] A similar procedure is performeed in computer graphics to scan a 3D graphic object using polynomial basis functions.

where $\mathcal{N} \triangleq 2N+1$.

The finite dimensional counter part of convolution operators [1] is circulant symmetric matrices representing circular convolution. However, circulant convolution produces magnetic coupling from the front to the rear of the track removing the end effect, which is undesirable. Instead, we truncated the inductive coupling at each end of the track creating *Toeplitz matrices* [25]. With the mentioned modifications, the $\mathcal{N}$-by-$\mathcal{N}$ track inductance matrix $\mathcal{L}_{\mathcal{N}}$ becomes

$$\mathcal{L}_{\mathcal{N}} \triangleq \begin{bmatrix} L & M_1 & \dots & M_{\mathcal{N}-2} & M_{\mathcal{N}-1} \\ M_1 & L & \dots & M_{\mathcal{N}-3} & M_{\mathcal{N}-2} \\ \vdots & \vdots & \ddots & \vdots & \vdots \\ M_{\mathcal{N}-2} & M_{\mathcal{N}-3} & \dots & L & M_1 \\ M_{\mathcal{N}-1} & M_{\mathcal{N}-2} & \dots & M_1 & L \end{bmatrix}, \tag{15}$$

where L is the loop self inductance, and M_n is the mutual inductance between two loops separated by $n-1$ loops [1].

Since the track is $D\mathcal{N} = D(2N+1)$ long, the *track sampling operator* $\Gamma^x_{\mathcal{N}D}(nD)$ for the periodic track model is a truncated version of the bi-infinite $\Gamma^x\{nD\}$ in (4) as

$$\Gamma^x_{\mathcal{N}}(nD) f(x, y_\phi) \triangleq \bigotimes_{n=-N}^{N} f(nD - x, y_\phi)|_{x-D}^{x'=x},$$

which is simply $\mathcal{N}$ translations in the x-direction with lattice constant D of the function $f(x', y_\phi)|_{x-D}^{x'=x}$. The $\Gamma^x_{\Delta\phi\mathcal{N}}(nD)$ operator is by analogy a truncation of the $\Gamma^x_{\Delta\phi}\{nD\}$ operator (5).

4 Periodic track model - Dynamic equations for numerical implementation

With the modifications in foregoing sections, we have tailored the ITM (1)-(3) according to the force continuity criterion (6) for numerical implementation, and have obtained the *periodic track model (PTM)*

$$\frac{d}{dt} i_0 = -\alpha dx_D/dt \, i_0 \tag{16}$$

$$\begin{aligned} \frac{d}{dt} i_{\mathcal{N}}(n) &= -\mathcal{L}_{\mathcal{N}}^{-1} \mathcal{R}_{\mathcal{N}} i_{\mathcal{N}}(n) + \mathcal{L}_{\mathcal{N}}^{-1} \Gamma^x_{\Delta\phi\mathcal{N}}(nD) \mathcal{B}_y^{sP}(x_D, y_\phi) \frac{dx_D}{dt} \\ &\quad -\mathcal{L}_{\mathcal{N}}^{-1} \Gamma^x_{\Delta\phi\mathcal{N}}(nD) \int \frac{\partial}{\partial y} \mathcal{B}_y^{sP}(x', y_\phi) dx' \frac{dy}{dt} \end{aligned} \tag{17}$$

$$\frac{d^2 x_D}{dt^2} = \frac{1}{m} \sum_{n=N-N^F}^{\mathcal{N}-\left(N-N^F\right)} \Gamma^x_{\mathcal{N}}(nD) \mathcal{B}_y^{sP}(x_D, y_F) i_{\mathcal{N}}(n) - \frac{1}{m} \left(\alpha_x^{par} + \alpha_x^m\right) \frac{dx}{dt} + \frac{1}{m} F_x^{in} \tag{18}$$

$$\frac{d^2 y}{dt^2} = -\frac{1}{m} \sum_{n=N-N^F}^{\mathcal{N}-\left(N-N^F\right)} \Gamma^x_{\mathcal{N}}(nD) \mathcal{B}_x^{sP}(x_D, y_F) i_{\mathcal{N}}(n) - \frac{1}{m} \left(\alpha_y^{par} + \alpha_y^m\right) \frac{dy}{dt} + \frac{1}{m} F_y^{in} - g, \tag{19}$$

where the inner product $\langle \{a_n\}, \{b_n\} \rangle_n$ in (2) and (3) are replaced by a finite sum over the force window. The Equations (16)-(19) are integrated according to the following algorithm:

Sequential Execution Algorithm of the PTM (16)-(19)

1. **Initiate**

$$\begin{aligned} 0 \le x(t_0) < D \\ m_x(t_0) = 0 \end{aligned} \tag{20}$$

2. **Run**

$$\begin{aligned} 0 < x_D(t) < D, \quad t \in [t_{m-1}, t_m] \\ m_x = m \end{aligned} \tag{21}$$

3. **Stop**

$$x_D(t_m^-) = D \tag{22}$$

4. **Reset**

$$\begin{array}{l} x_D(t_m^+) = 0 \\ m_x(t_m^+) = m_x(t_m^-) + 1 \\ i_{\mathcal{N}}(n, t_m^+) = i_{\mathcal{N}}(n+1, t_m^-), \quad n \in \{0, \ldots, \mathcal{N}-1\} \\ i_{\mathcal{N}}(\mathcal{N}, t_m^+) = i_0(t_m^-) \end{array} \tag{23}$$

5. **Goto 2**

The output current mapping from the PTM currents $i_{\mathcal{N}}(n,t)$ to the *track currents* $i^{track}(k,t)$, where k is between 1 and $\max(\mathcal{N}, m_x)$ is

$$i^{track}(k,t) = i_{\mathcal{N}}(l,t), \quad l = (k - m_x/\mathcal{N})_{\mathrm{mod}\,\mathcal{N}}. \tag{24}$$

The PTM (16)-(19) must be integrated with a variable time step solver capable of detecting the zero crossing $x_D(t_m^-) = D$ in the stop condition down to numerical accuracy of the FPU. Otherwise, there are force and current discontinuities from the reset other than the removed current $i_1(t_1^-)$, which error will propagate over time.

The PTM can also be integrated at fixed propulsion speeds v_x by fixing $x_D = (v_x t)_{\mathrm{mod}\,D}$ and ignoring (18). Similarly, levitation height can also be fixed $y = y^{const}$ by disregarding (19). However disregarding (18) and/or (19) yields a solution that is not on the solution manifold of the equations (1)-(3), as the full ITM does not have a critical point corresponding to constant levitation height y^{const} unless $\mathbf{F}^{in}$ is a very special periodic function. Drawing hastily conclusions from operating the model with reduced mechanical dynamics can lead to strange results, as the unstable propulsion dynamics found in [26] as criticized by [15].

4.1 Power balance and model accuracy

The magnetic energy E^J of the track currents $i_{\mathcal{N}}(n)$ is

$$E^J = \frac{1}{2}\, i_{\mathcal{N}}^T(n)\, \mathcal{L}_{\mathcal{N}}\, i_{\mathcal{N}}^T(n)\,. \tag{25}$$

Similarly, the *track dissipation power* $P^{\mathcal{RN}}$ is a finite sum incorporating the termination rung resistance R_T (13) as

$$P^{\mathcal{RN}} = R_T i_1^2 + \left(\sum_{n=2}^{\mathcal{N}} 2\, R_b i_n^2 + R_r (i_n - i_{n-1})^2 \right) + R_T i_{\mathcal{N}}^2. \tag{26}$$

Ignoring the mechanical damping coefficient $\boldsymbol{\alpha}^m = (\alpha_x^m, \alpha_y^m, 0)$ and the parasitic dissipation coefficient $\boldsymbol{\alpha}^{par} = (\alpha_x^{par}, \alpha_y^{par}, 0)$ yields a magnetic force

$$\mathbf{F} = \sum_{n=N-N_F}^{\mathcal{N}-(N-N_F)} i_{\mathcal{N}}(n)\, \hat{\mathbf{e}}_z \times \Gamma_{\mathcal{N}}^x(nD) \mathcal{B}^{sP}(x_D, y_F). \tag{27}$$

Together, (26) and (27) provide a measure to check the integration accuracy of the model by analyzing the electromagnetic power balance averaged over the time interval $[0, T]$ as

$$\frac{1}{T} \int_{\mathbf{p}(0)}^{\mathbf{p}(T)} \mathbf{F}\, d\mathbf{p} - \frac{1}{T} \int_0^T P^{\mathcal{RN}} dt = \varepsilon(T) + \epsilon^i, \tag{28}$$

where ϵ^i is a numerical error, and $\varepsilon(T) = E^J(T) - E^J(0)$. If we evaluate (28) on a periodic orbit[5] such that $(i_{\mathcal{N}}(n)(t), y(t)) = (i_{\mathcal{N}}(n)(t+T), y(t+T))$, we have that $\varepsilon(T) = 0$. Thus, the numerical error ϵ^i in (28) is available explicit.

[5] Here, we must allow all cyclic permutations of $i\{n\}$ to be equivalent to have periodic motion when for instance the levitated object has moved the distance between two track rungs D such that $T = D/v_x$.

The error ϵ in the force continuity criterion (6) is upper bounded based on the force discontinuity at reset $|\mathbf{F}_{N^F}(t_m^-) - \mathbf{F}_{N^F}(t_m^+)| = |\mathbf{f}_{N^F+1}(t_m^-)|$ as explained in Appendix 9.2. By defining the force error bound constant

$$\varsigma \triangleq 2\left(\frac{1}{1-e^{-D(k+1/v_x\tau)}} - e^{-D(k+1/v_x\tau)}\right), \tag{29}$$

the bound on the force error becomes

$$|\mathbf{F} - \mathbf{F}_{N^F}|_{l_1} \leq \epsilon < \varsigma \mathbf{f}_{N^F}(t_m^-). \tag{30}$$

and provides an upper bound on the force error between the ITM and the PTM in terms of the observed force discontinuity in the PTM.

4.2 Spline fit of the magnetic field

There are several practical issues pertaining to the spline fits that must be addressed in order to assure the force continuity (6).

First, the fit of $\mathcal{B}_x^{sP}$and $\mathcal{B}_y^{sP}$ are made on individual grids to have better control of the approximation error $\left|\mathcal{B}_k^s - \mathcal{B}_k^{sP}\right|$, as mentioned in Section 3.4, to prevent the error becoming excessively large.

Second, in order to avoid a derivative where $\int_0^Y (\partial/\partial y \mathcal{B}_y^{sP})dy \neq \mathcal{B}_y^{sP}(Y) - \mathcal{B}_y^{sP}(0)$, $\partial/\partial y \mathcal{B}_y^{sP}$ is evaluated by differentiating the spline $\mathcal{B}_y^{sP}$. This is performed off-line to save computation time. Assuring that $\int_0^Y (\partial/\partial y \mathcal{B}_y^{sP})dy = \mathcal{B}_y^{sP}(Y) - \mathcal{B}_y^{sP}(0)$ is particularly important for correct heave dynamics in (17)-(19).

Third, the evaluation of the integral $\int_{-D-x}^{-x} \partial/\partial y \mathcal{B}_y^{sP}(x', y_\phi)dx'$ in (17), depends on the location of the interval $[-D-x, -x]$ in the breakpoint sequence $(\xi_i)_{K+1}$, and must be performed on-line. This choice of implementation places an even greater restriction on the approximation error $\partial/\partial y \mathcal{B}_y^s(y) - \partial/\partial y \mathcal{B}_y^{sP}(y)$ which must be evenly distributed around zero to prevent the error from accumulating in the integral $\int_{-D-x}^{-x} \partial/\partial y \mathcal{B}_y^{sP}(x', y_\phi)dx'$.

As we use tensor product splines, where multiple dimensions are created by repeated application of a one dimensional spline fit [24], it is sufficient with one dimensional theory. The pp-form spline $s(x)$ used for evaluation on $x \in [\xi_1, \xi_{K+1}]$ subdivided into K intervals and separated by the break point sequence $(\xi_i)_{K+1}$ (11) has the representation

$$s(x) = \sum_{j=1}^{K} \Omega_j p_j(x), \quad \Omega_j = \begin{cases} 1, & x \in [\xi_j, \xi_{j+1}] \\ 0 & elsewhere, \end{cases} \tag{31}$$

where Ω_j is the characteristic function of the j-th interval. If $\partial/\partial y \mathcal{B}_y^{sP}$ should be once continuous differentiable, we must at least employ fourth order splines, hence $p_j(x)$ is a third order polynomial; whence the spline $s(x)$ becomes

$$s(x) = \sum_{j=1}^{K} \Omega_j \sum_{i=1}^{4} c_{ij} \left(x - \xi_j\right)^{4-i}, \tag{32}$$

and its derivative $s'(x)$ is

$$s'(x) = \sum_{j=1}^{K} \Omega_j \sum_{i=1}^{3} c_{ij} (4-i) \left(x - \xi_j\right)^{3-i}. \tag{33}$$

Integration over the interval $[a, b]$, where $\xi_m \leq a \leq \xi_{m+1}$ and $\xi_{m+n} \leq b \leq \xi_{m+n+1}$ becomes

$$\begin{aligned} \int_a^b s(x)dx \quad = \quad & \sum_{i=1}^{4} \left[\frac{c_{im}}{(5-i)} \left(\left(\xi_{m+1} - \xi_m\right)^{5-i} - \left(a - \xi_m\right)^{5-i} \right) \right. \\ & \left. + \left(\sum_{j=m+1}^{m+n-1} \frac{c_{ij}}{(5-i)} \left(\xi_{j+1} - \xi_j\right)^{5-i} \right) + \frac{c_{i(m+n)}}{(5-i)} \left(b - \xi_{m+n}\right)^{5-i} \right]. \end{aligned} \tag{34}$$

Two dimensional splines are created by first fitting K curves in the x-direction with the break point sequence $(\xi_i)_{K+1}$, thereafter we treat the coefficients in these splines as points c_{ijm} on lines in the y-direction with the break point sequence $(\zeta_i)_{J+1}$, where the one dimensional procedure can be repeated for these coefficient lines [24].

4.2.1 Spline fitting procedure

It is implicitly assumed that the spline fit is performed on the magnetic field with attenuated tails $\mathcal{B}^{cut}(x', y', z')$ as explained in Section 3.3, and hereafter $\mathcal{B}^{cut} = \mathcal{B}^s$ for notational convenience. The attenuated tails of $\mathcal{B}^s$ favorably commensurate with the requirement of zero boundary derivative of the splines, so it is not required to produce additional boundary derivatives[6]. In other words, a set of points S of the magnetic field $\mathbf{B}(x', y', z')$ is the data for the spline fit, and we assume that any measurement noise has been filtered out from S.

The lateral integration of the magnetic field components B_x^s and B_y^s into $\mathcal{B}_x^s$ and $\mathcal{B}_y^s$, is performed numerically using any quadrature formula as long as the approximation error ϵ is kept small. The choice of method depends on the number of lateral data points and their spacing. If the data points are taken on a uniform grid with grid constant Δz and $N_z + 1$ grid points in the z-direction, the rectangular approximation

$$\mathcal{B}_k^s(x, y) = \int_{-w/2}^{w/2} B_k^s(x', y', z')dz' = \Delta z' \sum_{n=1}^{N} B_k^s(x', y', \Delta z' n) + \epsilon^l, \tag{35}$$

will suffice if Δz is chosen sufficiently small to yield a small error ϵ^l.

The breakpoint sequences $(\xi_i)_{K+1}$ and $(\zeta_i)_{J+1}$ must be carefully chosen. Inadequate breakpoint sequences are excessively large, and slows down evaluation without reducing the approximation error compared to a properly selected shorter sequence. If one starts with an inappropriate $(\xi_i)_{K+1}$, the approximation error is not necessary reduced by introducing more points—the error can just as well increase. The selection of $(\xi_i)_{K+1}$ and $(\zeta_i)_{J+1}$ is something of an art, and some trial and error is required. To ease our burden, we should precondition the magnetic fields by smoothing out high spatial frequencies that are outside the region of interest.

4.2.2 Smoothing out high spatial frequencies

The magnetic field 5-10 mm away from the magnetic source is never used for computation due to the thickness of the rungs. This region contains high spatial frequencies as shown in Figure 4 which cause problems for the spline fit.

To remove these frequencies, we filter $\mathcal{B}_x^s$ and $\mathcal{B}_y^s$ in the x direction using a non-causal finite impulse response filter (FIR) to avoid the phase lag (distortion) of a causal filter. The filtered $\mathcal{B}_y^s$ is shown in Figure 5 and should be compared to the unfiltered $\mathcal{B}_x$ in Figure 4.The filter must also have unity dc-gain to prevent

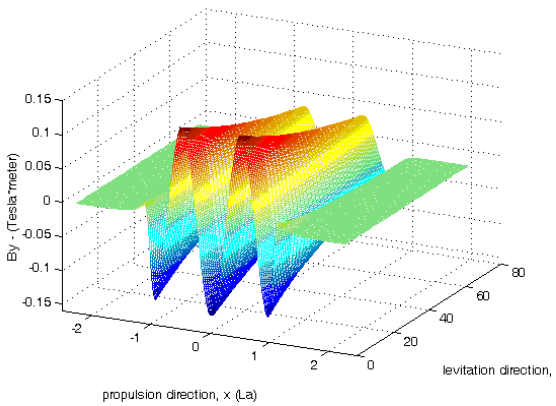

Figure 5: The transversely integrated vertical magnetic field $\mathcal{B}_y^s$ from the Halbach array shown in Figure 8 with details in Appendix 9.1. The field $\mathcal{B}_y^s$ was sampled on a 2 mm grid in the x-direction, and run through the filter (36) once with $Q = 20$ and $p = 0.9$.

amplification of the magnetic field. Many choices are available, but we choose a simple filter as off-line we

[6] This is under the agreement that the two uttermost breakpoints on both sides in the y-direction is chosen sufficiently far away from the region in which we whish to evaluate $\mathcal{B}(x', y')$.

can make the window size Q arbitrary large to improve the steepness of the cut. We can also reapply the filter for a sharper cut. The difference equation for our filter with input sequence $u(n)$ and output sequence $y(n)$ is

$$y(n) = g\left(\sum_{m=0}^{Q} p^m u(n-m) + \sum_{m=1}^{Q} p^m u(n+m)\right) \tag{36}$$

$$g = \tfrac{1-2p(a^Q+1)}{1-p}, \quad |p| < 1, \tag{37}$$

where increasing p removes more high frequency information, and Q should be kept large for a steep cut.

4.3 Properties of the PTM

By numerically integrating the PTM (16)-(19) according to the sequential execution algorithm, we obtain time dynamic forces F^l and F^d and currents $i_{\mathcal{N}}(n)(t)$ that can be made arbitrary close to the forces and current $i\{n\}(t)$ of the ITM (1)-(3). By including sufficiently many track conductors ascribed by (6), the force discontinuities from removing conductors can be made less than the solver tolerances as shown in Figure 6, so the dynamic properties of the PTM are exactly those of the ITM.

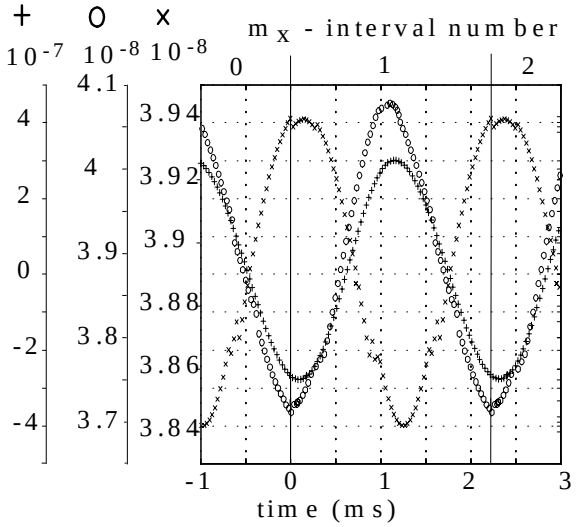

Figure 6: Numeric solution of the PTM displaying the lift force continuity x: $\left(F^l(t_n) - F^l(t_{n-1})\right)/F^l(t_n)$, the drag force continuity o: $\left(F^d(t_n) - F^d(t_{n-1})\right)/F^d(t_n)$, and the normalized power continuity (28) + : $\left(P^{\mathcal{RN}} - P^F\right)/P^{\mathcal{RN}}$. The force continuity error ϵ at interval switch (reset) is smaller than the largest force increment during normal integration.

The switching intervals between the time instances $\{t_0, t_1, t_3, t_4, \ldots\}$ are at constant speed $t_m - t_{m-1} = T^D = D/v_x$ apart, and generate the oscillations shown in Figure 6 from the track interspace D.

By removing all parasitic damping $\boldsymbol{\alpha}^{par}$ and mechanical damping $\boldsymbol{\alpha}^m$ in (18)-(19), the PTM has increasing heave oscillations at the natural levitation frequency $\omega_0 = \sqrt{2kg}$, $k = 2\pi/\lambda$ [18], as shown in Figure 7.

The track currents are best viewed at constant levitation height y time-scaled by the constant propulsion velocity v_x, normalized to λ and time-reversed as $i(-t\lambda/v_x)$ for comparison with the magnetic fields $\mathcal{B}_x$ and $\mathcal{B}_y$ as shown in Figure 8.

At constant propulsion speed and constant levitation height, the rung current in the track at any time instant is a time sample of a single rung current $i_n - i_{n-1}$ at intervals $T^D = D/v_x$. This enables the simplified LPM model derived in the next Section

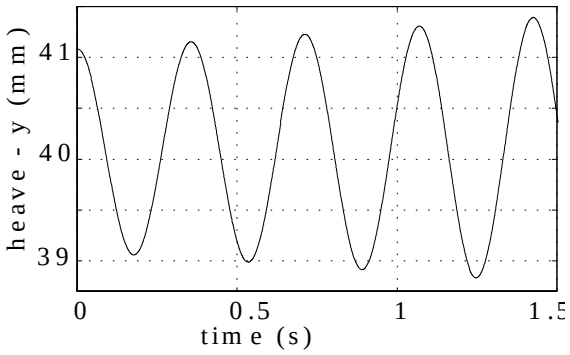

Figure 7: Unstable heave (levitation) in the absence of parasitic damping. $F^p = 1547.45N$ which gives an equilibrium propulsion velocity of 17.64 m/s. Equilibrium levitation height is $y = 4.00$ mm. The observed 'negative damping' is approximately 250 $N\ s/m$.

5 Lumped parameter model - equations for baseline design

Lumped parameter models (LPM) provide simple, but less accurate, formulas for baseline design. The order reduction is achieved by modifying the PTM through the following steps:

1. Parasitic dissipation is removed.
2. Propulsion speed is assumed constant.
3. Levitation height is fixed.
4. End effect of the track is ignored.
5. The magnetic source field is assumed periodic.

In what follows, step 3 can be relaxed by more elaborate time-scale analysis which preserves the heave dynamics which is the subject of [20].

Typically, in rudimentary investigations of continuous track EDS maglev, the mirror magnetic field in the track is assumed to be an exact mirror image of the primary field in order to make the mirror image stationary in the body attached reference frame. This analysis is not applicable for discrete tracks, where the current pattern is never independent of time (stationary) in the vehicle's reference frame $(\hat{\mathbf{e}}'_x, \hat{\mathbf{e}}'_y, \hat{\mathbf{e}}'_z)$ due to the spacing of track rungs. For discrete tracks, sampling the track current at time instances equally spaced by $T^D \triangleq D/v_x$ yields a stationary image in the moving reference frame. Equivalently, on the lattice (grid) $t - T^D m$ for integer m, the track current i_n conform to

$$i_{n+m}(t) = i_n(t - T^D m). \tag{38}$$

Equation (38) is referred to as the *Space-Shift Time-Shift Equivalence (SSTSE)*, and enables discrete track analysis without assuming a stationary current pattern. The SSTSE relies on constant levitation height, and constant propulsion speed; however, there is no requirement of periodicity in the magnetic field.

We now continue making the necessary assumptions for simplifying the magnetic field.

5.1 Simplified magnetic field

Even for short Halbach arrays, the magnetic field is close to sinusoidal, as shown in Figure 8, and the quality of this approximation improves with the number of wavelengths in the array [23]. In addition, the magnetic field decays rapidly outside the magnetic source window W^J as seen in Figure 8. Also notice that the currents decay quickly outside W^J, and that the track currents are nearly an amplified, phase shifted 'footprint' of $\mathcal{B}_y$. Consequently, the currents outside W^J contribute little to the lift force. So we shrink the track window W in Figure 2 to a phase-shift of the magnetic source window W^J, and have ignored the track end effect:

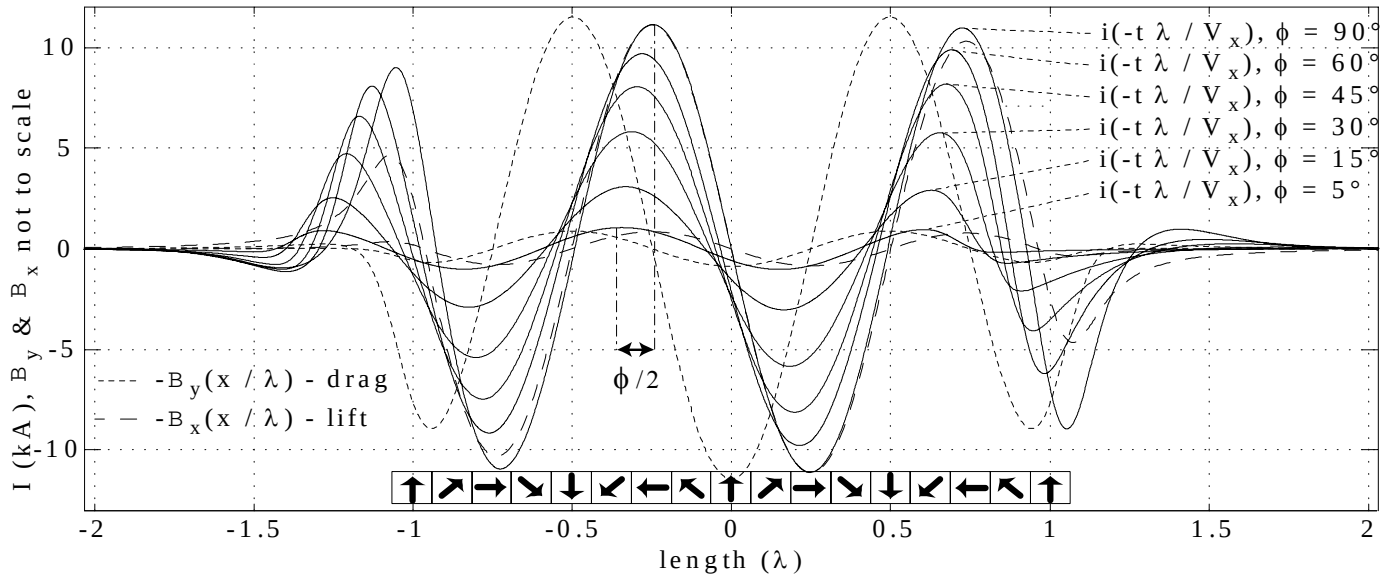

Figure 8: Scaled rung currents from the PTM at levitation height ($y = 22\,mm$) at different constant propulsion speeds v_x compared to the magnetic fields $\mathcal{B}_x(x, y = 22\ mm)$ and $\mathcal{B}_y(x, y = 22mm)$. Observe the current phase $\phi \triangleq \arctan(\frac{v_x}{v_t}) \in [0, 90)$ which shifts forwards with velocity. The shown length of the x-axis corresponds to W^F at $\phi = 45$.

Assumption 1 *Track currents outside the track window W are zero.*

For a double Halbach array, assumed to be infinitely long, the 2D analytic expression for the magnetic flux density is given by Halbach in [27], Equation (5). For a single array with remanent magnetic field B_r, with N bars per wavelength λ, each with a thickness d, this formula becomes

$$\mathbf{B}(x', y') = B_0 e^{-nky'} \sum_{v=0}^{\infty} (\hat{\mathbf{e}}_x \sin nkx' + \hat{\mathbf{e}}_y \cos nkx') \tag{39}$$

$$B_0 = B_r(1 - e^{-nkd}) \frac{\sin n\epsilon\pi/N}{n\pi/N} \tag{40}$$

$$k = \tfrac{2\pi}{\lambda}, \quad n = 1 + vN \ , \tag{41}$$

where $\epsilon\lambda/N$ is the length of a single magnet block, so that $\epsilon = 1$ if there is no spacing between the blocks. In the survey article [28], Equation (6), Halbach points out that retaining the first harmonic in (39) is a good approximation. The resulting magnetic field is

$$\mathcal{B}(x', y') \approx \mathcal{B}_0 e^{-ky'_\phi} \left[\sin(kx')\hat{\mathbf{e}}_x + \cos(kx')\hat{\mathbf{e}}_y\right], \tag{42}$$

and should be compared with the magnetic field $\mathcal{B}^s$ in Figure 8. Unfortunately, the 2D approximation the formula is based on is equivalent to assuming that the array is infinitely wide. So for the approximation to hold, we should require that the width of the Halbach array $\mathbf{w}^s$ is much wider than the track w, or $w^s/w >> 1$. This is rarely the case in maglev applications, so the coefficient B_0 (40) cannot be used for computing the flux [23]. Halbach do not provide analytic formulas for the flux over a region, since it is merely the magnitude of the flux density in the transverse center of the array that is of interest for linear undulators.

To remedy this, we derive the coefficient $\mathcal{B}_0$, obtained by transverse integration of the field, from 3D field considerations computed by FEM or analytic solution as in [23]. With this modification, (42) is a good approximation, and we have made the assumption:

Assumption 2 *The magnetic source field is infinitely long, and only the first harmonic in the field is retained.*

Here, we have ignored the high frequency components close to the array for heights $y < \lambda/(2N)$, and neither is this approximation valid for the far field [22],[23].

Now, it suffices to consider a set of $\mathcal{N}_\lambda$ currents $\{i_1, \ldots, i_{N_\lambda}\}$ below a wavelength of Halbach array, since a current i_n leaving W^J in Figure 2 is replaced by the current i_{n+N_λ} entering W^J in front, because the currents one wavelength away are identical, or $i_n = i_{n+N_\lambda}$. The mild technical assumption this relies on is:

Assumption 3 *The wavelength of the source λ is divisible by the conductor spacing D, and the Halbach array contains an integer number of wavelengths.*[7]

We are left with $\mathcal{N}_\lambda$ track currents, so that the track operators $\mathcal{R}_{N_\lambda}$ and $\mathcal{L}_{N_\lambda}$ are now $\mathcal{N}_\lambda$-by-$\mathcal{N}_\lambda$ matrices, but we have also introduced flux coupling from rear to front (by ignoring the end effect) generating *circulant symmetric* matrices as

$$\mathcal{L}_{N_\lambda} \triangleq \begin{bmatrix} L & M_1 & \ldots & M_2 & M_1 \\ M_1 & L & \ldots & M_3 & M_2 \\ \vdots & \vdots & \ddots & \vdots & \vdots \\ M_2 & M_3 & \ldots & L & M_1 \\ M_1 & M_2 & \ldots & M_1 & L \end{bmatrix}. \tag{43}$$

These matrices are the finite dimension counterpart of convolution operators like $\mathcal{L}$ and $\mathcal{R}$ which do not have any eigenvectors [29]. The eigenvectors of finite dimensional circulant symmetric matrices form the Fourier matrix $\mathcal{F}$ whose (k,l) element $f_{k,l}$ is given by

$$f_{k,l} \triangleq \frac{1}{\sqrt{N_\lambda}} e^{j\theta kl}, \quad \theta \triangleq \frac{2\pi}{N_\lambda},$$

which is determined solely by the circulant symmetry, and is independent of the values of the elements in the matrix [25]. Therefore, we are not adding artificial properties (like electrical modes) to the track by using circular symmetric matrices like (43).

We have now gone through all the steps in the introduction of Section 5, and are left with $\mathcal{N}_\lambda$ currents $\{i_1, \ldots, i_{N_\lambda}\}$ below a wavelength of Halbach array. We continue the reduction in Section 5.2 to a single *equivalent loop current* i_n with scalar *lumped inductive reactance* L_{eq} and *lumped resistance* R_{eq} replacing the matrices $\mathcal{L}_{N_\lambda}$ and $\mathcal{R}_{N_\lambda}$, respectively. In Section 5.3, the static force equation without the summation from the inner product in (2) and (3) is derived. Both these reductions are facilitated by the SSTSE (38).

5.2 Lumped parameter electric equation with L_{eq} and R_{eq}

One limitation with the LPM is that it is difficult to account for $\Delta\phi$ and yet retain the simplicity of the equations. Consequently, for double-sided sources either F^l or F^d is reliable when $\Delta\phi = 0$, which necessitates two sets of equations to account for both F^l and F^d. Such equations can be extrapolated from the derivation that follows, and we restrict our derivation to a single-sided source as displayed in Figure 9.

The e.m.f. around the n-th ladder track loop E_n in Figure 9 becomes after substituting in the periodic

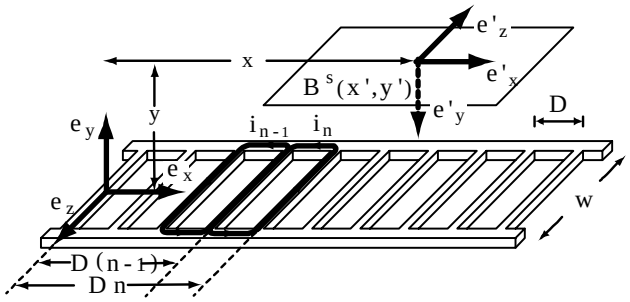

Figure 9: Schematic of the stationary frame (x, y, z) and the body fixed (moving) frame (x', y', z').

[7] This assumption can be omitted if we use averaging instead of summation to derive the governing equations.

magnetic field (42)

$$E_n(x, y_\phi) = \mathcal{B}_0 A e^{-ky_\phi} \left(-\cos(kx - \psi(n)) \frac{dx}{dt} + \sin(kx - \psi(n)) \frac{dy}{dt} \right), \tag{44}$$

where $A = 2\sin(\frac{kD}{2})$, and the angle $\psi(n) = kD(2n-1)/2$ is fixed for given n and is ignored.

Kirchhoff's voltage law for the n-th filament loop is

$$R^{loop} i_n + \sum_m l_m \frac{d}{dt} i_{n+m} = E_n(x, y_\phi). \tag{45}$$

Equation (45) depends on the current in the neighboring loops i_{n+m} which we replace by time shifts of a single current i_n from the SSTSE $i_{n+m}(t) = i_n(t - T^D m)$. The e.m.f. from track flux coupling becomes

$$\sum_m l_m \frac{d}{dt} i_{n+m} = \sum_m l_m \frac{d}{dt} i_n(t - T^D\, m). \tag{46}$$

We have assumed that the heave y_ϕ is constant so that $E_n(x, y_\phi) = E_n(x)$ is a periodic function. Since equation (45) is a linear ODE, periodicity in E_n implies periodicity in i_n; since E_n is sinusoidal, i_n is also sinusoidal. Therefore. $i_n(t - T^D m)$ is a phase shift of $i_n(t)$ as $i_n(t - T^D m) = e^{-jkDm} i_n(t)$, and the voltage contribution from inductive reactance (46) becomes

$$\left(l_0 + \sum_{m \neq n} l_m e^{-jkDm} \right) \frac{d}{dt} i_n(t). \tag{47}$$

The summation remains purely real from the complex conjugate symmetry between indices $+m$ and $-m$, so we define the expression inside the brackets as the *lumped parameter track inductance* L_{eq}

$$L_{eq} \triangleq l_0 + 2 \sum_{m=1}^{\infty} l_m \cos kDm. \tag{48}$$

Formula (48) commensurate with the derivations in [16], [5], [17], and is a constant if the wavelength of the Halbach array λ is divisible by the rung spacing D, which we have assumed in Assumption 3.

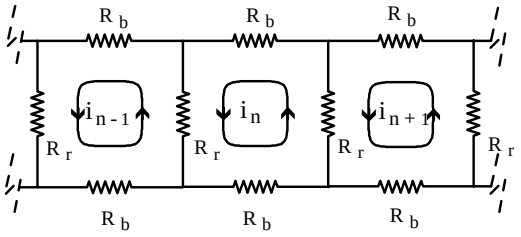

Figure 10: Schematic of the resistance network for a ladder track.

From Figure (10) we derive the loop resistance for the ladder track

$$R_{loop} = 2R_b i_n + R_r \left(2i_n - i_{n-1} - i_{n+1}\right), \tag{49}$$

which we rewrite using the SSTSE (38) as above, and define the loop resistance as the *lumped parameter track resistance* R_{eq}

$$R_{eq} = 2\left(R_b + R_r(1 - \cos kD)\right). \tag{50}$$

The *track electric equation* is now simply Faraday's Law (45) for the equivalent track circuit with only one track current i_n

$$R_{eq} i_n + L_{eq} \frac{di_n}{dt} = E_n. \tag{51}$$

Having justified the lumped parameter model with only one track coil, we have replaced the PDE for the track current (1) with a simple R-L circuit as shown in Figure (11) which represents Faraday's Law (51).

Notice that L_{eq} (48) depends on the mean spacing of track rungs D through $\cos kDm$, and on the wavelengths in the Halbach array through $k = 2\pi/\lambda$. So L_{eq} is not determined solely by the track, but is also affected by the source magnetic field. Equation (48) is also the sum of a purely oscillating sequence $\{\cos kDm\}$ and a slowly decaying sequence $\{l_n\}$, hence the product $l_m \cos kDm$ settles very slowly, and an appropriate numerical approximation of L_{eq} must retain sufficiently many terms (10^3) in the infinite sum in (48).

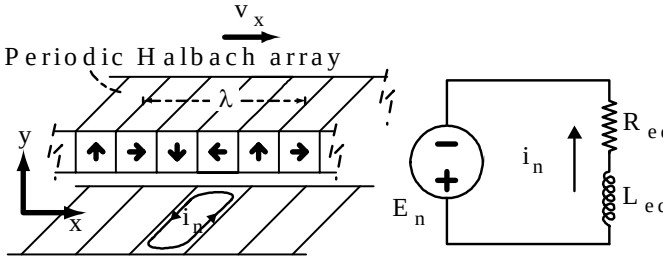

Figure 11: Equivalent R-L circuit for the lumped parameter track equation (51).

Further similarities between (1) and (51) are revealed by solving the later equation with the e.m.f. from a single-sided source (44), at constant propulsion velocity $dx/dt = v_x$, and constant levitation height $y_\phi = y$. By defining the *transition speed* v_t as

$$v_t \triangleq \frac{R_{eq}}{kL_{eq}}, \tag{52}$$

and the *phase angle* ϕ

$$\phi \triangleq \arctan(\frac{v_x}{v_t}) \in [0, \tfrac{\pi}{2}), \tag{53}$$

the solution to (51) with zero initial condition is

$$\begin{aligned} i_n(t) &= \frac{\mathcal{B}_0\sqrt{2}\sin(kD)e^{-ky_\phi}v_t}{R_{eq}}\sqrt{\gamma(\phi)} \\ &\quad \left(\cos(kv_x t - \phi) - \frac{1}{\sqrt{\gamma(\phi)}}e^{-\frac{R_{eq}}{L_{eq}}t}\right), \end{aligned} \tag{54}$$

where the factors $\gamma(\phi)$ and $\zeta(\phi)$ are defined as

$$\gamma(\phi) \triangleq \frac{1}{1+\left(\frac{v_t}{v_x}\right)^2} = \frac{1}{2}\left(1-\cos 2\phi\right) \tag{55}$$

$$\zeta(\phi) \triangleq \frac{\frac{v_t}{v_x}}{1+\left(\frac{v_t}{v_x}\right)^2} = \frac{1}{2}\sin 2\phi. \tag{56}$$

Notice that ϕ is the angle between the voltage E_n and the current i_n in the one loop equivalent circuit in Figure 11. More importantly, $\phi/2$ **is the phase lag of the mirror magnetic field in the track from the source magnetic field**[8] as indicated in Figure 8. In the next Section we will see that v_t is the speed where the lift force equals the drag force under constant levitation height.

[8]This convention is with opposite directed y-axis (heave) for the source and the mirror magnetic field accounting for the minus sign in Lenz' Law.

5.3 Lumped parameter static forces replacing the mechanical equation

It remains to reduce the sum in the mechanical equations (2) and (3) to an expression of the same single current i_n. Under the assumptions of constant propulsion speed $x = v_x t$, and constant levitation height y_ϕ, the total force $\mathbf{F}$ from N^λ conductors under a wavelength of the Halbach array equals

$$\mathbf{F} = \sum_{m=0}^{N_\lambda - 1} i_{n+m}(t)\hat{\mathbf{e}}_z \times \mathcal{B}(mD - v_x t, y_F), \tag{57}$$

where we have substituted the vertical position of the n-th loop in the moving frame x' resolved in the stationary frame $x^{'} = mD - x$ according to Figure 9. By ignoring the transient part $e^{-tR_{eq}/L_{eq}}$ in (54), and using the SSTSE for the sinusoidal current, the force becomes

$$\begin{aligned}\mathbf{F} &= \frac{\mathcal{B}_0^2 \sin(\frac{kD}{2}) e^{-k(y_\phi + y_F)}}{kL_{eq}} \gamma(\phi) \left(\sum_{n=0}^{N^\lambda - 1} \cos(kv_x t - kDn - \phi) \right. \\ &\left. [\sin(kv_x t - kDn)\hat{\mathbf{e}}_x + \cos(kv_x t - k)\hat{\mathbf{e}}_y] \right). \end{aligned} \tag{58}$$

Performing the summation over a wavelength, and defining the constant G

$$G\left(y_\phi + y_F\right) = \frac{\mathcal{B}_0^2 \sin(\frac{kD}{2}) N^\lambda e^{-k(y_\phi + y_F)}}{kL_{eq}}, \tag{59}$$

the lift force F^l and the drag force F^d per wavelength of array become

$$F^l = \frac{G}{2}\left[(1 - \cos 2\phi) + \epsilon \sin 2kv_x t\right] \tag{60}$$

$$F^d = -\frac{G}{2}\left[\sin 2\phi + \epsilon \sin 2kv_x t\right]. \tag{61}$$

The small term $\epsilon = \sin^2 2\pi(\lambda - N^\lambda D)$ is zero if the wavelength λ of the Halbach array is divisible by the conductor spacing D as in Assumption 3. If we average the force $\langle F(t)\rangle_{\lambda/v_x}$, ϵ will disappear when v_x is sufficiently high regardless of Assumption 3, and the corresponding ripple will not appear in the lift- and drag forces.

Neglecting ϵ, equation (60) and (61) are identical to the force expressions for continuous sheet track in [15][9], where $v_0 = v_t$, $F_\infty = G$, which is valid for an "infinitesimal thin, perfectly conducting track of finite conductivity per square", the *thin sheet - high speed limit*, as clarified in [30]. It should be explicitly noted that these expressions neglect the skin effect and are therefore overly optimistic at high speeds. To include the skinning effect, we must add a term proportional to v_x/v_t in the drag force, set to $k^2 d^2 v_x / 6v_t$ in [31] for continuous tracks with one-sided sources (normal flux).

6 Comparison between PTM and LPM

A comparison of the forces from the PTM and LPM is shown in Figure 12. Even though the shape of the forces versus speed are astonishingly similar (mean square error less than 1%), the parameters predicted by the LPM deviates form the best fit of the parameters k, G, v_t from the PTM. For the LPM these parameters are (with the best fit PTM parameters in brackets): $k = 14.32\ rad/s$ ($15.93\ rad/s$), $G = 24\ 225$ ($23\ 922$), and $v_t = 3.98\ s$, ($4.23\ s$ at $y = 20\ mm$ to $4.00\ s$ at $y = 80\ mm$). This might lead us to believe that the LPM can predict forces sufficiently accurate for the final design. This is incorrect, and a caution is appropriate concerning using lumped parameters and ignoring the end effect as this leads to several "judgement coefficients" which are impossible to determine a priori, reducing the prediction power of the LPM

For instance, the coefficient $\mathcal{B}_0$ in (42) is determined from the peaks of $\mathcal{B}_x$ and $\mathcal{B}_y$ shown with correct ratio in Figure 8. However, there are several peaks of different magnitude, and since both F^l and F^d contain the factor $\mathcal{B}_0^2$, they are very sensitive to incorrectly chosen $\mathcal{B}_0$. Knowing the accurate answer from the PTM, we

[9] Unfortunately, the authors calls this the "low-velocity limit" which is missleading. The ambiguity arises from the two spatial quantities for continuous tracks: d –track thickness– and λ, and their magnitude relative to v_x.

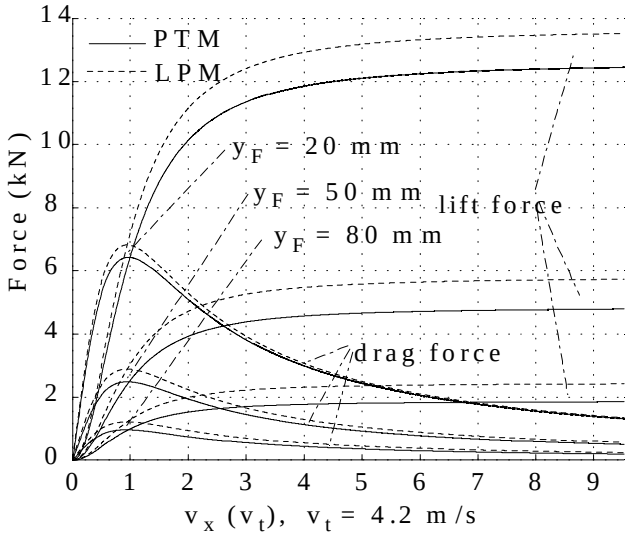

Figure 12: Comparison of PTM and LPM at $y_F = 20, 30, 80\ mm$, $\Delta y_\phi = 6\ mm$, $\Delta\phi = 0$ for the single sided Halbach array shown in Figure 8 and described in Appendix 9.1.

have chosen $\mathcal{B}_0$ according to the lowest of the peaks of $\mathcal{B}_y(x, y = 20mm)$ in Figure 8. Still, the LPM forces are too high, and if we had used the average peak height of $\mathcal{B}_y(x, y = 20mm)$, the forces had been 70% in excess. Therefore the LPM is less accurate in force magnitude predictions than shown here[10], and without guidance of an exact answer when choosing the "judgement coefficient" $\mathcal{B}_0$, the force magnitude of the LPM have an inaccuracy of at least ±30%. However, v_t in (52) is more accurate, but the wave number k provided by the fundamental wavelength λ, is 10% too low due to the end effect, which causes incorrect dependence on the levitation height y.

7 Conclusion

We have derived numerical equations for discrete track electrodynamically suspended (EDS) maglev from the infinite track model (ITM) presented in [1], and have provided an explicit bound on the deviation of the numerical equations, named the periodic track model (PTM), relative to the ITM. The PTM employs resetting of the state, and incorporates spline approximations of the conditioned source magnetic field.

Through simulations we have demonstrated that in the absence of damping from eddy currents, the ITM has unstable heave dynamics, and the rung currents at constant speed and levitation height resembles velocity scaled, phase shifted versions of the current inducing magnetic field.

The main benefits of the PTM are:

- Arbitrary accurate dynamic precision in the computed forces and currents, achieved through a careful derivation without unjustified approximations.
- The model accounts for field coupling between track conductors, and provides a mean to account for the end effect without running out of track.
- The source magnetic field is derived from the precise geometry of the source currents, and no assumptions are made on the source currents.
- The PTM provides a dynamic simulation building block in the Simulink environment useful for constructing larger dynamical simulations.

We have also derived a lumped parameter model (LPM) from the PTM, and have clearly stated the underlying assumptions. The LPM has an equivalent circuit with lumped inductance and resistance where

[10] This coroborates with General Atomics experience on their Urban maglev project.

the phase shift between the current and the voltage resembles the phase shift observed in the PTM. The LPM's static force formulas versus propulsion velocity have the same shape as the continuous track thin sheet and high speed approximation.

We show through simulations that, given the right coefficients, the LPM have a very similar behavior as the PTM, but the main inaccuracy in the LPM arise from the difficulty of determining the coefficients a priori.

8 Acknowledgements

We wish to express our gratitude to the General Atomics' urban maglev development team for their cooperation. This material is based upon work supported by the National Science Foundation under Grant no. CMS-0220386.

Quantity	Symbol	Value	Unit
wavelength of Halbach array	λ	0.4385	m
wave number of Halbach array	$k = \frac{2\pi}{\lambda}$	14.32	rad/s
width of the Halbach array	w^s	0.25	m
length of the Halbach array	L^s	2*0.4635	m
magnetic source window	W^J	2*0.4908	m
force window	W^F	2*1.052	m
track window	W	2*1.551	m
levitated weight	m	660	kg
track width	w	0.5	m
center spacing between track rungs	D	39.26	mm
force offset height from rung center	Δy_F	0	mm
flux offset height from rung center	Δy_ϕ	6	mm
flux increase parameter	$\Delta\phi$	0	mm
sidebar resistance	R_b	1.325	$\mu\Omega$
rung resistance	R_r	31.25	$\mu\Omega$
rung self inductance	L_r	0.48	μH
LPM equivalent inductance	L_{eq}	0.219	μH
LPM equivalent resistance	R_{eq}	12.5	$\mu\Omega$
LPM transition speed	v_t	3.98	s
LPM force constant	G	$24*10^3$	-

Table 1: Physical parameters taken from the General Atomics rotating wheel facility.

9 Appendix

9.1 Simulation details

In all PTM simulations the magnetic source was a one-sided, five blocks wide Halbach array with NdFeB magnets with bar orientation displayed in Figure 8. The two transverse outer blocks had a remnant field strength of 1.01 $Tesla$ (MEOMAX$^{\text{TM}}$ 37) whereas the three transverse center blocks had a remnant field strength of 1.32 $Tesla$ (NEOMAX$^{\text{TM}}$ 48). All magnet blocks were cubes with sides 50 mm, and the interspace between blocks was 4.5 mm. The magnetic field was computed using magnetization sheets as described in [23],[22].

The PTM was solved in the Simulink environment with a Runge-Kutta 4-5 solver with zero detection, and the error tolerance was selected based on the propulsion speed. The constant in the force error bound was $\zeta = 2.9595$ (66). A typical $\mathbf{f}_{N_F}(t_m^-)$ is shown in Figure 6 and is of the order 10^{-9}. The parasitic damping $\boldsymbol{\alpha}^{par}$ and the mechanical damping $\boldsymbol{\alpha}^m$ were zero in all simulations. The remaining parameters are given in Table 1.

9.2 Evaluating the force continuity

We assume that we have included $\mathcal{N}^F = 2N^F + 1$ currents in our model in accordance with Section 3.5, so that the neglected currents are $\{\ldots, i_{-N-2}, i_{-N-1}, i_{N+1}, i_{N+2}, \ldots\}$. The force from the included currents is denoted $\mathbf{F}_{N_F} = \sum_{n=-N_F}^{N_F} \mathbf{f}_n$, where $\mathbf{f}_n = (\mathbf{i}_n - \mathbf{i}_{n-1}) \times \mathcal{B}$ is the partial force from rung number n. At each solver reset instant t_m, there is a force continuity error from the removed rear current $i_{-N}(t_m^-)$ equal to

$$\left|\mathbf{F}_{N^F}(t_m^-) - \mathbf{F}_{N^F}(t_m^+)\right| = \left|\mathbf{f}_{N^F}(t_m^-)\right| = \sup_{t\in[t_m, t_{m+1}]} \left|\mathbf{f}_{N^F}(t)\right|, \tag{62}$$

If we now make the assumptions that all currents outside the force window decay at the rear and grow in front as $i_n \sim e^{\pm t/\tau}$, $\tau = R_{eq}/L_{eq}$, and that the magnetic field outside W^F decays as $\mathcal{B} \sim e^{-kx}$, then the partial force decays as $\mathbf{f}_n \sim e^{-kx - t/\tau}$ away from W^F. If we assume constant speed v_x in the time interval $[t_m, t_{m+1}]$, we have that $t = D/v_x$. In addition, $x = Dn$ such that the partial force not accounted for in the PTM is

$$\mathbf{f}_{N^F+n} = \mathbf{f}_{N_F} e^{-Dn(k + 1/v_x\tau)}. \tag{63}$$

The error between the force of the ITM and the PTM is

$$\sum_{\substack{n\in\mathbb{Z}\\ |m|\leq N^F}} |\mathbf{f}_n - \mathbf{f}_m| = \sum_{\substack{n\in\mathbb{Z}\\ |n|>N^F}} |\mathbf{f}_n| = 2\sum_{n=N^F+1}^{\infty} |\mathbf{f}_n|\,, \tag{64}$$

where the last equality follows from using the current at the rear of the array to approximate those in front which is reasonable considering Figure 8. Inserting (63) into (64), and summing the geometric series $\left\{e^{-Dn(k+1/v_x\tau)}\right\}$ yields

$$2\,|\mathbf{f}_{N^F}|\sum_{n=1}^{\infty} e^{-Dn(k+1/v_x\tau)} = \varsigma\mathbf{f}_{N^F}(t_m^-), \tag{65}$$

where the constant ς is defined as

$$\varsigma \triangleq 2\left(\frac{1}{1-e^{-D(k+1/v_x\tau)}} - e^{-D(k+1/v_x\tau)}\right). \tag{66}$$

Finally, we arrive at the explicit bound on the total force error in the l_1 norm as

$$|\mathbf{F} - \mathbf{F}_{N^F}|_{l_1} \leq \epsilon < \zeta\mathbf{f}_{N^F}(t_m^-), \tag{67}$$

in terms of the observed force discontinuity $\mathbf{f}_{N^F}(t_m^-)$. In other words, by observing $\mathbf{f}_{N^F}(t_m^-)$ in a simulation, we can compute the upper bound on the maximum force error ϵ.

10 Bibliography

References

[1] O. F. Storset and B. E. Paden, "Discrete track electrodynamic maglev part i: Modeling," *IEEE Transactions on Magnetics*, 2005. Submitted.

[2] K. Watanabe, H. Yoshioka, and E. Suzuki, "Combined control of primary and secondary suspension of maglev vehicles," *Quarterly Reports of RTRI (Japanese Railway Technical Research Institute)*, vol. 45, pp. 26–31, Feb. 2004.

[3] D. M. Rote, "Passive damping in EDS maglev systems," in *17th International Conference on Magnetically Levitated Systems and Linear Drives (MAGLEV'2002), Lausanne, Switzerland*, (Lausanne, Switzerland), Sep. 3-5, 2002.

[4] A. V. Baiko, K. Voevodskii, and V. M. Kochetkov, "Vertical unstable stability of electrodynamic suspension of high-speed ground transport," *Cryogenics*, vol. 20, pp. 271–6, 1980.

[5] H. T. Coffey, F. Chilton, and L. O. Hoppie, "The feasibility of magnetically levitating high speed ground vehicles," Final Report, Task I U S National Technical Inormation Service Publication nb. 210 505, US Federal Railroad Administration Report no. PB 210 505, Stanford Research Institute, Menlo Park, California 94025, USA, February 1972. Identical to NTIS PB 221696.

[6] C. A. Guderjahn, S. L. Wipf, H. F. Fink, R. N. Boom, K. E. MacKenzie, D. Williams, and T. Downey, "Magnetic suspension and guidance for high speed rockets by superconducting magnets," *Journal of Applied Physics*, vol. 40, pp. 2133–40, April 1969.

[7] J. L. He, D. M. Rote, and H. T. Coffey, "Applications of the dynamic circuit theory to maglev suspension systems," *IEEE Transactions on Magnetics*, vol. 29, pp. 4153–64, Nov. 1993.

[8] J. L. He, H. T. Coffey, and D. M. Rote, "Analysis of the combined maglev levitation, propulsion, and guidance system," *IEEE Transactions on Magnetics*, vol. 31, pp. 981–7, March 1995.

[9] M. Andriollo, G. Martinelli, A. Morini, and A. Scuttari, "Transient stability in EDS-MAGLEV vehicles: Numerical simulations," in *Proc. 14th Int. Conf. Magnetically-Levitated Systems*, (Bremen, Germany), pp. 455–459, Nov, 26-29 1995.

[10] N. Carbonari, G. Martinelli, and A. Morini, "Calculation of levitation, drag and lateral forces in EDS-MAGLEV transport systems," *Archiv fur Elektrotechnik*, vol. 71, no. 2, pp. 139–48, 1988.

[11] M. Andriollo, G. Martinelli, M. F. Moisio, and A. Morini, "Calculation of propulsion forces in EDS-maglev transport systems with superconducting coils," *Archiv fur Elektrotechnik*, vol. 72, no. 5, pp. 333–9, 1989.

[12] K. Higashi, S. Ohashi, H. Ohsaki, and E. Masada, "Magnetic damping of the electrodynamic suspension-type superconducting levitation system," *Electrical Engineering in Japan*, vol. 127, pp. 49–60, July-Aug. 1999. English Translation of Denki Gakkai Ronbunshi, vol. 117D, no. 8, Aug. 1997, pp. 1015-23.

[13] S. Ohashi, H. Ohsaki, and E. Masada, "Equivalent model of the side wall electrodynamic suspension system," *Electrical Engineering in Japan (English Translation of Denki Gakkai Ronbunshi)*, vol. 124, pp. 63–73, July 1998.

[14] D. M. Rote and Y. Cai, "Review of dynamic stability of repulsive-force maglev suspension systems," *IEEE Transactions on Magnetics*, vol. 38, pp. 1383–390, March 2002.

[15] P. L. Richards and M. Thinkham, "Magnetic suspension and propulsion systems for high-speed transportation," *Journal of Applied Physics*, vol. 43, pp. 2680–91, June 1972.

[16] L. O. Hoppie, F. Chilton, H. T. Coffey, and R. C. Singleton, "Electromagnetic lift and drag forces on a superconducting magnet propelled along a guideway composed of metallic loops," *Proceedings of the 5th Applied Superconductivity Conference, Annapolis, MD (USA)*, p. 113, 1972.

[17] E. Ohno, M. Iwamoto, and T. Yamada, "Characteristics of superconductive magnetic suspension and propulsion for high-speed trains," *Proceedings of the IEEE*, vol. 61, pp. 579–86, May 1973.

[18] R. F. Post and D. D. Ryutov, "The Inductrack: A simpler approach to magnetic levitation," *IEEE Transactions on Applied Superconductivity*, vol. 10, pp. 901–904, March 2000.

[19] O. F. Storset and B. E. Paden, "Discrete track electrodynamic maglev part III: Experimental data and model validation," *IEEE Transactions on Magnetics*, 2005. Submitted.

[20] O. F. Storset and B. E. Paden, "Dynamics of electrodynamic maglev," *Journal of Dynamic Systems, Measurement and Control.*, 2005. Submitted.

[21] A. F. Filippov, *Differential Equations with Discontinuous Righthand Sides*. Boston, USA: Kluwer Academic Publishers, 1988.

[22] J. F. Hoburg, "Modeling maglev passenger compartment static magnetic fields from linear Halbach permanent-magnet arrays," *IEEE Transactions on Magnetics*, pp. 59–64, 2004.

[23] O. F. Storset and B. E. Paden, "Computing the magnetic field from Halbach arrays," *IEEE Transactions on Magnetics*, 2005. Submitted.

[24] C. de Boor, *A Practical Guide to Splines*. New York: Springer Verlag, 1978.

[25] H. Widom, *Toeplitz Matrices*, vol. 3 of *Studies in Mathematics*, ch. 8, pp. 179–209. Englewood Cliffs, New York: Prentice-Hall, Inc., 1 ed., 1965.

[26] L. C. Davis and D. F. Wilkie, "Analysis of motion of magnetic levitation systems: Implications for high-speed vehicles," *Journal of Applied Physiscs*, vol. 42, pp. 4779–93, Nov. 1971.

[27] K. Halbach, "Physical and optical propperties of rare earth cobalt magnets," *Nuclear Instruments and Methods*, no. 187, pp. 109–17, 1981.

[28] K. Halbach, "Applications of permanent magnets in accelerators and electron storage rings," *Journal of Applied Physics*, vol. 57, pp. 3605–8, April 1985.

[29] O. F. Storset and B. Paden, "Infinite dimensional models for perforated track electrodynamic maglev," *41st IEEE Conference on Decision and Control*, pp. 842–847, Dec. 2002.

[30] S. W. Lee and R. C. Menendez, "Forces at high and low speed limits in magnetic levitation systems," *Journal of Applied Physics*, vol. 46, pp. 422–5, Jan. 1975.

[31] L. Urankar, "Forces on null-flux magnetic levitation systems," *Journal of Applied Physics*, vol. 44, pp. 1907–8, April 1973.